ISOBARIC ANALOG STATES IN RARE-EARTH NUCLEI STUDIED WITH THE (³He, t) CHARGE-EXCHANGE REACTION AT $\theta_L = 0°$

J. JÄNECKE

Department of Physics, University of Michigan, Ann Arbor, Michigan 48109, USA

and

Kernfysisch Versneller Instituut, 9747 AA Groningen, The Netherlands

E. H. L. AARTS, A. G. DRENTJE and M. N. HARAKEH

Kernfysisch Versneller Instituut, 9747 AA Groningen, The Netherlands

and

C. GAARDE

Niels Bohr Institute, DK-2100 Copenhagen Ø, Denmark

Abstract: The (³He, t) charge-exchange reaction leading to the ground-state isobaric analog states (IAS) of ^{152,154,156,158,160}Gd, ^{160,162}Dy, ^{162,164,166,168,170}Er, ^{170,172,174,176}Yb and ^{176,178,180}Hf has been studied at $\theta_L = 0°$ and $E(^3He) = 60.5$ MeV. The reaction ^{28}Si(³He, t)^{28}P was used for energy calibration. The centroid energies of most IAS were determined to ± 6 keV. Coulomb displacement energies have been extracted from the measured Q-values. They display the influence of non-spherical nuclear shapes which increase the rms radii and lower the Coulomb displacement energies. The dependence on both quadrupole *and* hexadecapole deformations is apparent with deformation parameters in good agreement with results from other measurements. The total widths Γ of the IAS are in the range 30 to 110 keV. They increase more strongly with neutron excess than is known for the IAS of the Sn and Te isotopes. The width of the IAS of ^{176}Yb is anomalously low. The zero-degree (³He, t) cross sections are in the range 5 to 20 μb/sr. They generally increase with neutron excess except for the sequence of Yb isotopes. No systematic dependence on $(N-Z)$ appears to exist. Excitation energies and zero-degree cross sections for the reactions ^{28}Si(³He, t)^{28}P, ^{16}O(³He, t)^{16}F and ^{12}C(³He, t)^{12}N are reported.

1. Introduction

Coulomb energies of atomic nuclei depend on their size and shape. Historically, one of the earliest estimates of nuclear charge radii was obtained by Bethe[1]) based

on the electrostatic energy difference between the ground states of mirror nuclei. Muonic X-ray and electron scattering experiments[2-6] have contributed significantly over the years to the understanding of the size and shape of nuclear charge distributions. After the discovery[7] of isobaric analog states (IAS) in heavy nuclei additional information has come from Coulomb energy differences[6,8,9]. These energies are sensitive to the charge distribution and to the distribution of the excess neutrons. Small additional contributions to the experimental displacement energies have been recognized and have become the subject of detailed theoretical studies[9-13]. However, typically 95% of the experimental Coulomb displacement energies encompass the direct Coulomb energy contributions which, when reasonable assumptions about neutron radii are made, provide basic information about the nuclear charge distribution. This is evident, for example, for the deformed rare-earth nuclei. It has been noted repeatedly[8,14,15] that the direct Coulomb energy of deformed nuclei is reduced by the approximate factor $1 - \beta_2^2/4\pi$ where β_2 is the quadrupole deformation parameter. Indeed, reductions with respect to estimates for spherical nuclei of up to 150 keV have been observed experimentally but quantitative analyses are scarce[14-16]. The influence of the hexadecapole deformation β_4 has never been established. Quantitative information about the deformation of nuclear charge distributions has been derived primarily from muonic X-ray and electron scattering experiments. However, only inelastic scattering, Coulomb excitation and Coulomb/nuclear interference experiments have yielded deformation parameters higher than β_2. Characteristics of the charge deformation parameters β_2, β_4 and β_6 of the rare-earth nuclei have been discussed recently[17]. Sizes and shapes of nuclear charge distributions are, of course, intimately related to other distributions including those for neutron and nucleon matter as well as interaction potentials (optical potentials).

It was the objective of the present work to measure Coulomb displacement energies of deformed nuclei with the highest possible precision in order to establish the effect of the hexadecapole deformation of the nuclear shape. It was in part stimulated by the results of Merril et al.[15] who observed an unexplained weak local maximum within the deformation minimum. It occurs near the region where β_4 is known to change sign. The region $A = 150$ to 180 was chosen for the investigation.

The two most important types of reactions to determine Coulomb displacement energies are the (p, n) and (^{3}He, t) charge-exchange reactions and proton-resonance reactions. It appears that essentially all existing data for rare-earth targets were obtained from proton-resonance experiments on even-A targets yielding displacement energies for odd-A systems. We have used the (^{3}He, t) reaction on 19 even-A targets to obtain precision data for even-A systems. Possible complications in the interpretation due to odd-even staggering effects are thus avoided. The experimental results also allow determination of IAS widths and zero-degree cross sections of the charge-exchange reaction which provide nuclear structure information.

2. Experimental procedures

A beam of 60.5 MeV ^{3}He^{++} particles from the KVI cyclotron was used for the measurements. The beam current was typically 200 nA. The beam upon entering the magnetic spectrograph at $\theta_L = 0°$ was bent inward and stopped in a graphite beam stop mounted at the end of an aluminum baffle. A monitor detector was mounted in the scattering chamber at $\theta_L = 25°$ to monitor beam current and target thickness. Tritons from the (^{3}He, t) reaction were detected in the focal plane of the QMG/2 magnetic spectrograph[18]) which was set for a solid angle of 6 msr. The baffle to stop the ^{3}He beam did not interfere with the tritons which have higher magnetic rigidity. The experimental arrangement is similar to one used earlier[19]) in a study of isobaric analog states of tin and tellurium isotopes.

The focal-plane detection system[20]) consists of two thin (~ 1 cm) position-sensitive proportional counters placed ~ 10 cm apart to allow ray tracing. They also provide energy loss signals. They are backed by a scintillator detector which generates light output and time-of-flight signals. Tritons are identified without background from other reaction products. It was sufficient to use only one of two such detection systems which are mounted in the focal plane of the spectrograph

TABLE 1

Targets

Nucleus	Enrichment (%)	$\rho\Delta x$ [a]) (μg/cm^2)	Carbon backing $\rho\Delta x$ [b]) (μg/cm^2)	Comments [c])
^{152}Gd	32.2	34	65	
^{154}Gd	71.4	109	39	
^{156}Gd	93.6	94	76	
^{158}Gd	97.6	72	70	
^{160}Gd	94.0	83	29	
^{160}Dy	68.5	285	43	
^{162}Dy	91.0	146	55	
^{162}Er	100.0	$15 \pm 20\%$	81	spot target
^{164}Er	100.0	$33 \pm 15\%$	80	spot target
^{166}Er	94.9	107	75	
^{168}Er	95.2	81	37	
^{170}Er	96.1	85	36	
^{170}Yb	67.2	164	46	
^{172}Yb	97.1	175	77	
^{174}Yb	99.0	86	36	
^{176}Yb	97.8	135	53	
^{176}Hf	100.0	$23 \pm 15\%$	54	spot target
^{178}Hf	94.7	168	78	sputtered
^{180}Hf	98.2	315	81	sputtered

[a]) Relative uncertainty $\pm 5\%$, absolute uncertainty $\pm 20\%$.
[b]) Relative uncertainty $\pm 10\%$, absolute uncertainty $\pm 30\%$.
[c]) All targets obtained by evaporation in vacuum except where noted.

side by side. The useful energy range was $\Delta E/E \approx 0.08$ which made it possible to take all data without changing the magnetic field settings. The experimental energy resolution for states with small intrinsic width was 20 keV due mostly to target thickness.

The 19 targets used are listed in table 1. Most targets were obtained by evaporating isotopically enriched material; two were obtained by sputtering; three are spot targets obtained by mass separation. Most target materials are enriched to $>95\%$ (see table 1), and most target thicknesses $\rho\Delta x$ are in the range 70 to 170 $\mu g/cm^2$. All targets have carbon backings of thickness 30 to 80 $\mu g/cm^2$. The thicknesses listed in the table are accurate to $\pm 5\%$ (absolute $\pm 20\%$). The uncertainty for the carbon backings is $\pm 10\%$ (absolute $\pm 30\%$). The mass thicknesses were determined by measuring proton-induced X-rays and by elastic scattering.

Since it was intended to obtain very precise values for the $(^3He, t)$ Q-values, the relative and absolute energy calibration and the influence of systematic effects required special attention. These considerations are presented in the next section.

3. Energy calibration

The reaction $^{28}Si(^3He, t)^{28}P$ has been used for energy calibration. Fig. 1 shows one of four calibration spectra which were taken at the beginning, during and at the end of the running period. Seven ^{28}P states were included in the fitting procedure excluding the weak 0^+ (877 keV) state, the $2^+/1^+$ (1516/1567 keV)

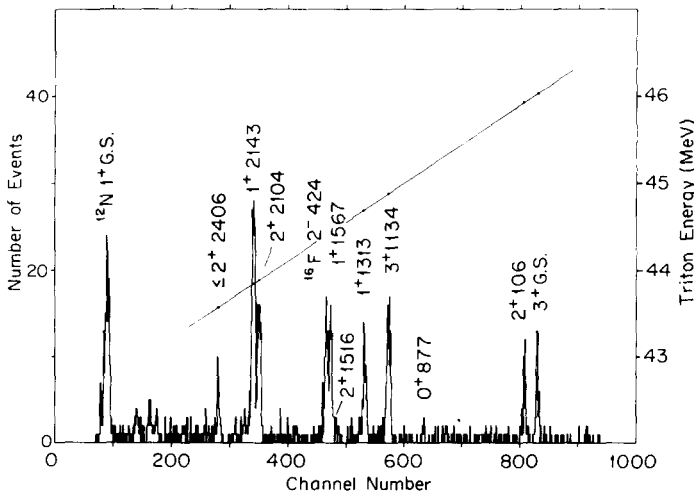Fig. 1. Spectrum of tritons from the calibration reaction $^{28}Si(^3He, t)^{28}P$ at $E(^3He) = 60.5$ MeV and $\theta_{lab} = 0°$.

doublet which is distorted by the presence of the nearby 2^- state in ^{16}F from small oxygen contaminations, and the weak 4^+ (3^+) (2216 keV) state. (See table 3 for the relative intensities.) The IAS from the various rare-earth targets were measured at the same magnetic field. The states lie between channel numbers 340 and 670 and thus well within the range of ^{28}P states used for the calibration. The ^{28}Si(^{3}He, t)^{28}P reaction provided an ideal calibration reaction for the relative measurements. The uncertainty of its Q-value of ± 3.7 keV which is the result of (p, n) Q-value measurements [21,22]) contributes to the absolute uncertainty.

A relativistic kinematics program was used to calculate the triton ejectile energies for the calibration and all other reactions. Masses of neutral atoms [23]) were used to calculate ground-state Q-values, and the excitation energies for ^{28}P were taken from ref. [24]). Contributions due to the difference in atomic binding energies or the degree of ionization of the residual nucleus are negligible. The triton energies were calculated using ion masses for both projectiles and ejectiles.

Two effects lead to measurable decreases of the ejectile energies, the energy loss in the target and the influence of the finite solid angle. These energies were subtracted from the calculated energies for ^{28}Si(^{3}He, t)^{28}P before the calibration procedure was carried out. Accordingly, they were added to the energies obtained for the IAS peaks and for ^{16}O(^{3}He, t)^{16}F before the Q-values were determined.

The (zero-degree) energy loss corrections were calculated from $\Delta E = \frac{1}{2}(\Delta E(^3\text{He}) + \Delta E(\text{t}))$ using the measured target thicknesses. They are about 10 keV for the Si target, and they range from about 1 to 15 keV for the rare-earth targets.

Energy corrections due to the finite solid angle are the result of second-order effects. First-order effects disappear for all targets since $(1/p)(\mathrm{d}p/\mathrm{d}\theta) = 0$. The corrections are easy to calculate because all spectra including the calibration spectra were measured at identical magnetic field settings including the multipole corrections. Ejectile energies near zero degrees are given by $E(\theta) = E_0 - \alpha\theta^2$ where α depends on target mass. The coefficients α can be calculated from kinematics, and for (^{3}He, t) on targets with $A = 12$, 16, 28, ~ 166 and ∞ we find $\alpha = 4.09$, 3.09, 1.73, 0.29 and 0.0 keV/deg^2, respectively. If the magnetic field is set to focus particle groups for an infinitely heavy target, then ejectiles from a finite-mass target will be shifted towards lower $B\rho$ for all angles $\theta \neq 0$. The centroid energy for a given solid angle is obtained by integrating over the horizontal and vertical angular ranges $\phi = \phi_0 \pm \Delta\phi$ and $\theta = \theta_0 \pm \Delta\theta$. Assuming constant cross sections over the entire solid angle, the result for rectangular geometry and $\phi_0 < \Delta\phi$, $\theta_0 < \Delta\theta$ is

$$\langle E \rangle = E_0 - \Delta E = E_0 - \alpha(\phi_0^2 + \tfrac{1}{3}\Delta\phi^2 + \theta_0^2 + \tfrac{1}{3}\Delta\theta^2). \tag{1}$$

For the geometry employed ($\Delta\Omega = 6.0$ msr), the finite solid angle correction is $\Delta E \approx 13.3$, 7.4 and 1.2 keV for ^{16}O, ^{28}Si and rare-earth targets, respectively. As the magnetic field was actually set to focus tritons from the rare-earth targets, the respective differences were used as corrections.

The correction given by eq. (1) has to be modified if the cross section varies as a function of angle. An explicit analytical expression shows that the correction may decrease or increase by at most 10–20 % for any reasonable variation in cross section. Realistic estimates have been made for a select number of isobaric analog states and states in ^{28}P and ^{16}F by calculating angular distributions based on assumed configurations. These estimates are included below, but they are very small and only for states in ^{16}F do the deviations from eq. (1) slightly exceed 1 keV.

The centroids for the seven selected peaks in each of the four calibration spectra (see fig. 1) were obtained with the peak-fitting program VIZFIT[25]). A least-squares fit was subsequently used to determine the calibration constants a and b in an expression linear in momentum,

$$E = (an + b)^2. \tag{2}$$

Here, E is the corrected calculated triton energy. The beam energy was $E_1 = 60.5 \pm 0.2$ MeV. The uncertainty of ± 200 keV contributes a negligible uncertainty of ± 0.2 keV to the resulting Q-values of the isobaric analog states (± 1.2 keV for ^{16}O(^{3}He, t)^{16}F). The quality of the calibrations is excellent, and eq. (2) with the fitted coefficients a and b reproduces the measured peaks with standard deviations of 2.0 to 2.5 keV. No peak deviates by more than 4 keV. The quoted uncertainties for the ^{28}P excitation energies range from 0.5 to 5 keV (see table 3).

The four calibration spectra display a systematic shift equivalent to about 10 keV from the beginning to the end of the running period. The origin of this effect is not entirely clear but may be due to a drift in beam energy. In order to compensate for this drift, small time-dependent terms were added to the coefficients a and b. The quality of the calibration eq. (2) remains excellent with possible systematic shifts of at most 0.5 keV.

The above calibration was subsequently used to determine ejectile energies for the IAS as well as states in ^{16}F. The corrected energies were then converted to Q-values. The results for the IAS are presented in the next section; those for ^{16}F are included in the appendix.

4. Experimental results

4.1. SPECTRA

Several typical position spectra for the (^{3}He, t) reaction at $\theta_{lab} = 0°$ are displayed in fig. 2. Whereas the measured spectra cover a range in excitation energies of about 3.5 MeV, fig. 2 shows only more limited ranges of 1.0 MeV near the IAS. All spectra have similar characteristics. The main features are the ground-state IAS, up to three ^{16}F states and the ^{12}N ground state (outside the range of interest)
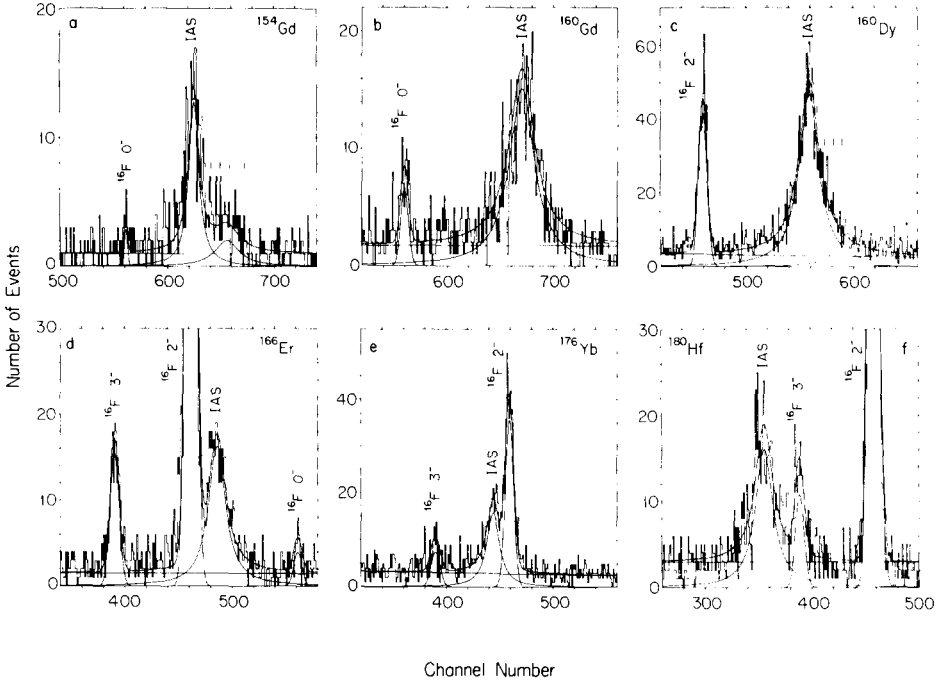
Fig. 2. Triton spectra from the (^{3}He, t) reaction at $E(^3$He) = 60.5 MeV, θ_{lab} = 0° leading to isobaric analog states (IAS) of selected rare-earth targets. The spectra display lines from oxygen contaminants. The thin continuous lines are from the line fitting program IGPLOT[26].

together with a weak background extending over the entire range. The background, rising slightly with increasing excitation energy, is in large part due to pickup/breakup or breakup/pickup reactions such as (^{3}He, tp) as well as direct and indirect excitations of $T_<$ states. Undistorted IAS transitions are shown in figs. 2b and 2f. They have lorentzian line shapes and are broader than the contaminant lines which are well fitted by gaussian line shapes. In a few cases, such as shown in figs. 2d and 2e, the IAS has to be unfolded from a nearby contaminant line leading to increased uncertainties. Another difficulty is the presence of isotopes of different mass. The ^{154}Gd and ^{160}Dy targets, for example, were only enriched to about 70 %, and the high-energy bumps in figs. 2a and 2c are clearly due to the heavier isotopes. Here, the yield from the heavier isotopes is enhanced due to the increase in cross section with neutron number (see fig. 7). Unfolding was again performed and peak positions, line widths and yields were determined with the peak fitting programs VIZFIT[25]) and IGPLOT[26]).

All targets are statically deformed nuclei with the first excited 2^+ state at about 80 keV. Excited analog states can be populated by one-step and two-step processes including inelastic excitations in the entrance or exit channels. No indications for such transitions could be found. At θ_{lab} = 0° they are apparently suppressed relative to the strongly favored $l = 0$ transitions to the 0^+ ground-state IAS.

The yield of ^{16}F states depends on the degree of oxidization in the respective target. Fig. 2d includes three ^{16}F states, 0 (g.s.), 2$^-$ (424 keV) and 3$^-$ (720 keV). The 2$^-$ state is by far the most intense. The 1$^-$ (194 keV) state is extremely weak (see appendix and table 3).

4.2. Q-VALUES. COULOMB DISPLACEMENT ENERGIES. IAS WIDTHS AND CROSS SECTIONS

Table 2 displays the experimental results. The uncertainties given for the Q-values reflect upon the estimated accuracy of the correction and fitting procedures. The precision of the calibration as well as the uncertainty in the Q-value of the reference reaction ^{28}Si(^{3}He, t)^{28}P. The uncertainties for Q and ΔE_{Coul} are therefore absolute.

TABLE 2

(^{3}He, t) reaction Q values, Coulomb displacement energies, IAS widths and zero-degree cross sections

Isobaric pair	A	Q (keV)	ΔE_C (keV)	Γ (keV)	$\dfrac{d\sigma}{d\Omega}$ (c.m.) (μb/sr)
$_{64}$Gd–$_{65}$Tb	152	-15421 ± 9	16184 ± 9	42 ± 12	6.1 ± 1.5
	154	-15348 ± 6	16112 ± 6	67 ± 8	11.6 ± 1.3
	156	-15280 ± 6	16044 ± 6	72 ± 9	13.9 ± 1.6
	158	-15205 ± 6	$15969 + 6$	81 ± 12	15.9 ± 2.4
	160	-15144 ± 6	15908 ± 6	100 ± 9	15.0 ± 1.7
$_{66}$Dy–$_{67}$Ho	160	-15647 ± 6	16410 ± 6	68 ± 10	17.3 ± 2.7
	162	-15585 ± 6	16349 ± 6	74 ± 9	18.7 ± 2.1
$_{68}$Er–$_{69}$Tm	162	-16097 ± 16	16861 ± 16	30 ± 23	< 16.4
	164	-16024 ± 9	16788 ± 9	43 ± 18	12.1 ± 3.6
	166	-15983 ± 7	16747 ± 7	69 ± 8	13.0 ± 1.5
	168	-15912 ± 6	16676 ± 6	106 ± 8	12.8 ± 1.4
	170	-15825 ± 6	16588 ± 6	104 ± 8	18.2 ± 2.0
$_{70}$Yb–$_{71}$Lu	170	-16333 ± 6	17096 ± 6	75 ± 21	12.6 ± 3.2
	172	-16271 ± 7	17035 ± 7	91 ± 16	10.4 ± 1.2
	174	-16198 ± 9	16962 ± 9	94 ± 15	7.8 ± 1.6
	176	-16151 ± 6	16915 ± 6	54 ± 9	5.2 ± 0.6
$_{72}$Hf–$_{73}$Ta	176	-16624 ± 7	17388 ± 7	75 ± 24	13.8 ± 3.7
	178	-16593 ± 6	17357 ± 6	85 ± 8	17.9 ± 2.0
	180	-16543 ± 7	17307 ± 7	87 ± 8	16.3 ± 1.8

The Coulomb displacement energies ΔE_{Coul} of table 2 have been deduced from the experimental Q-values using

$$\Delta E_{Coul} = -Q(^3\text{He, t}) + \Delta E_{Coul}(^3\text{He, t}). \qquad (3)$$

Here, $\Delta E_{Coul}(^3\text{He, t}) = 763.8$ keV [ref. [23])] is the Coulomb displacement energy
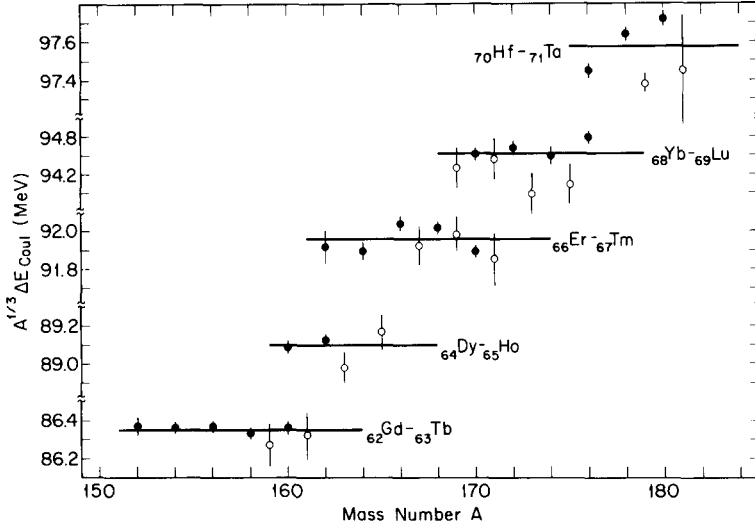
Fig. 3. Systematics of Coulomb displacement energies; plot of $A^{\frac{1}{3}}\Delta E_{\text{Coul}}$ versus mass number A. Data for even-A (filled circles) are from this work, for odd-A (open circles) from ref. [27].
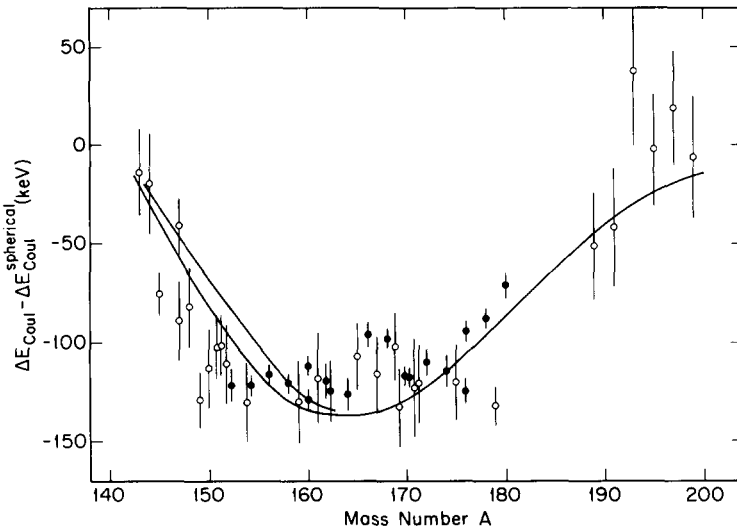

Fig. 4. Difference of Coulomb displacement energies for deformed and spherical nuclei as function of mass number A. The calculated curves are from eqs. (5) and (6) with calculated [17] deformation parameters β_2 and β_4 for nuclei along the line of stability. The lower curve includes the effect of hexadecapole deformation β_4.
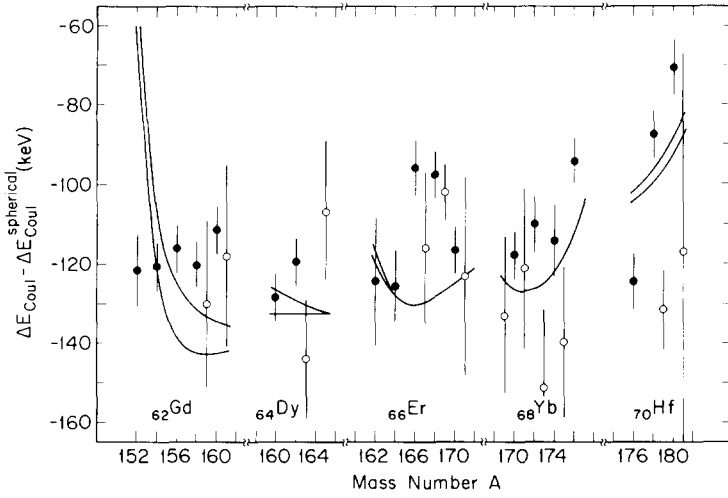
Fig. 5. Difference of Coulomb displacement energies for deformed and spherical nuclei as function of mass number A. The calculated curves are from eqs. (5) and (6) with experimental deformation parameters β_2 and calculated parameters β_4. Upper curves with $\beta_4 = 0$; lower curves with $\beta_4 \neq 0$.
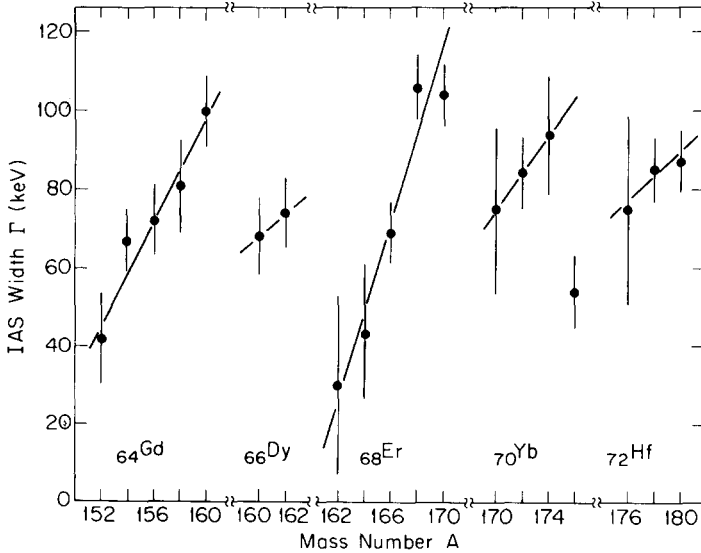

Fig. 6. Total widths Γ of isobaric analog states as function of mass number. The straight lines are included to guide the eye.
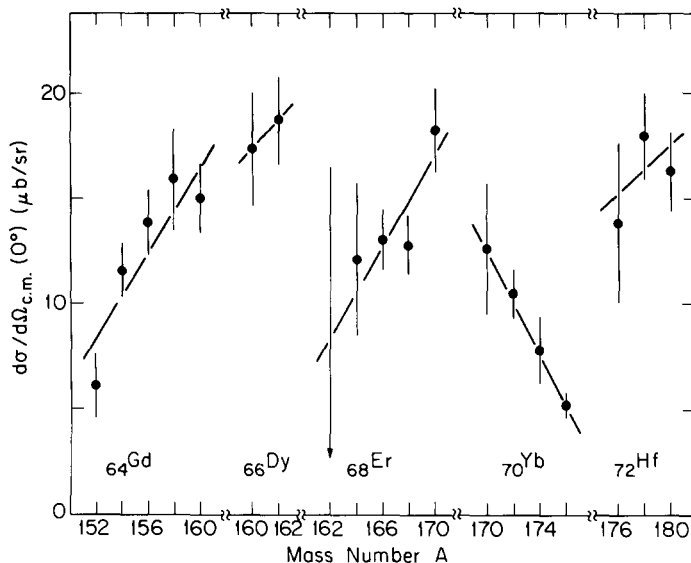
Fig. 7. Cross sections of (^{3}He, t) charge-exchange reactions at $E(^3$He$) = 60.5$ MeV and $\theta_{lab} = 0°$ leading to isobaric analog states. The straight lines are included to guide the eye.

between the mirror nuclei ^{3}He and ^{3}H. The data are displayed in figs. 3, 4 and 5 as $A^{\frac{1}{3}} \Delta E_{Coul}$ and $\Delta E_{Coul} - \Delta E_{Coul}$(spherical). The figures will be discussed below.

The total IAS widths Γ of table 2 have been deduced from the observed IAS peaks (see fig. 2) by unfolding the experimental line widths. They range from about 30 to 110 keV, generally increasing with neutron excess. They are plotted in fig. 6 as a function of mass number. The (^{3}He, t) charge-exchange cross sections at $\theta_{lab} = 0°$ are displayed in fig. 7 as a function of mass number. Ranging from 5 to 20 μb/sr, the cross sections generally increase with neutron excess except for the Yb isotopes which exhibit a pronounced decrease.

5. Calculation of Coulomb energies of deformed nuclei

The experimental Coulomb displacement energy for a single isobaric pair cannot be used to extract more than one parameter of the distributions of the charge and the excess neutrons. One therefore has to consider the systematic behavior of the displacement energies and make use of information obtained by other techniques. The emphasis in the present investigation is on the dependence of Coulomb displacement energies on nuclear shapes. An obvious approach is therefore to compare the displacement energies for deformed and spherical nuclei.

The dependence on proton and nucleon number of Coulomb displacement energies of spherical nuclei is quite well understood[8,9,28]. This is particularly true

for the direct Coulomb displacement energy, which encompasses about 95 % of the total energy, but the characteristics of smaller contributions from the exchange and the electromagnetic spin-orbit interaction are also well known. However, there are numerous small additional contributions from Coulomb perturbations, finite size charge-dependent nuclear forces, isospin impurities etc. which have been estimated only for a few select nuclei. Moreover, it also appears that the origin of the Nolen-Schiffer anomaly[9]) is still not fully understood[29]). The dependence on proton and nucleon number of these contributions is poorly understood. The sequence of Pb isotopes represent one such example where the effects have been estimated[9,13]) only for ^{208}Pb.

Whereas an analytical expression has been derived for the Coulomb energies of spherical nuclei with diffuse surfaces[28]), the "corrections" were included only in a phenomenological way. It was therefore decided in the present analysis to use a simple 2-parameter equation to describe the displacement energies of spherical nuclei,

$$\Delta E_{\text{Coul}}(Z, A) = a \frac{Z_<}{A^{\frac{1}{3}}} + b. \tag{4}$$

This expression is remarkably accurate[8]). It can also be modified to include the effect of deformed shapes by multiplying the first term with a deformation-dependent correction factor $1 - C(\beta_2, \beta_4)$. Such a factor should in principle contain shape, radius and diffuseness parameters for the proton core and the neutron excess[30]). A simpler expression[31]) which neglects diffuseness corrections and assumes equal deformation for proton core and neutron excess was considered sufficient. The expression derived by Hasse[31]),

$$1 - C(\beta_2, \beta_4) = 1 - B_2^2 - \tfrac{4}{21}\sqrt{5}B_2^3 + \tfrac{255}{49}B_2^4 - \tfrac{18}{7}B_2^2 B_4 - \tfrac{5}{3}B_4^2 \tag{5}$$

with $B_2 = \beta_2/(4\pi)^{\frac{1}{2}}$, $B_4 = \beta_4/(4\pi)^{\frac{1}{2}}$, contains corrections due to hexadecapole deformation β_4 to second order but corrections due to quadrupole deformation β_2 to fourth order. This is necessary because the latter are considerably bigger than the former.

Introducing eq. (5) into eq. (4) leads to a simple analytical expression for the difference of Coulomb displacement energies for nuclei with deformed and spherical shapes,

$$\Delta E_{\text{Coul}} - \Delta E_{\text{Coul}}^{\text{spherical}} = -a \frac{Z_<}{A^{\frac{1}{3}}} C(\beta_2, \beta_4). \tag{6}$$

Using experimental or calculated deformation parameters β_2 and β_4, eq. (6) provides a direct comparison with the experimental Coulomb displacement energies.

This assumes, though, that parameters a and b for eq. (4) can be found which reliably describe the energies of spherical nuclei.

Experimental deformation parameters β_2 and β_4 [see refs. [17,32,33]] are the result of electron scattering, muonic X-ray and other experiments. The quadrupole parameter β_2 reaches a maximum value of about 0.3 in the region $A = 160$. The hexadecapole parameter β_4 varies between $+0.07$ and -0.07; the sign changes near $A = 165$. Simple analytical expressions which describe the experimental deformation parameters β_2, β_4 and β_6 as a function of proton and neutron number have been derived recently [17]) for the region of rare-earth nuclei. Fig. 8 displays the
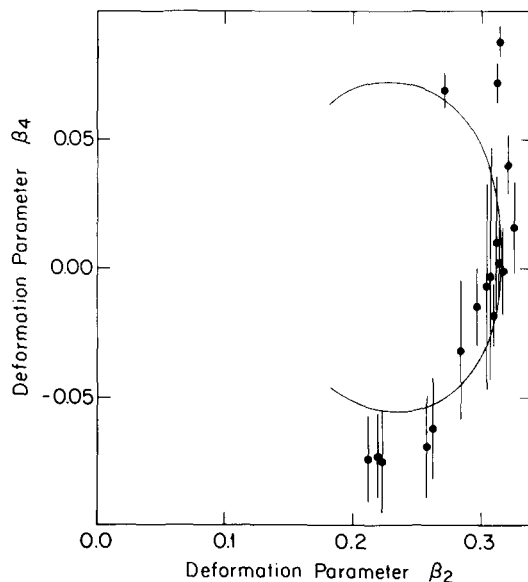

Fig. 8. Correlation between the experimental deformation parameters β_4 and β_2 for deformed rare-earth nuclei. The curve is calculated [17]) for nuclei along the line of stability eq. (7).

correlation between the experimental β_2 and β_4 for the rare-earth nuclei together with a curve based on the simple parameterization. The latter curve was calculated for the line of stable nuclei defined by

$$N - Z = \frac{0.4A^2}{200 + A} \, . \tag{7}$$

Both, experimental and calculated deformation parameters have been used in the subsequent section in conjunction with eqs. (4)–(7) to discuss the experimental Coulomb displacement energies.

6. Discussion

6.1. COULOMB DISPLACEMENT ENERGIES

Coulomb displacement energies for sequences of isotopes are expected to decrease approximately as $A^{-\frac{1}{3}}$ due to the increase of the radius with nucleon number. Fig. 3 displays for the five isobaric pairs investigated in this work the product $A^{\frac{1}{3}}\Delta E_{\mathrm{Coul}}$ as a function of mass number A. Indeed, except for the $_{70}$Hf isotopes, the data can be well described by horizontal lines. However, the isotopic lines are not equally spaced as expected from a more systematic behavior; the lines for $_{64}$Dy and $_{68}$Yb are about 60 keV lower than average. The influence of deformed shapes should actually lead to deviations from the simple $A^{-\frac{1}{3}}$ dependence. The deformation increases significantly for the $_{62}$Gd isotopes and decreases for the $_{70}$Hf isotopes. Coulomb displacement energies should therefore decrease more rapidly than $A^{-\frac{1}{3}}$ for the former, and less rapidly than $A^{-\frac{1}{3}}$ for the latter. Only the latter effect is observed, and the fact that $A^{\frac{1}{3}}\Delta E_{\mathrm{Coul}}$ is approximately constant for the $_{62}$Gd isotopes is unexpected.

Fig. 3 includes a few data[27]) for isobaric pairs with $A = $ odd (open circles). There is no obvious odd-even staggering except possibly for the $_{68}$Yb and $_{70}$Hf isotopes where the odd-A data tend to be lower.

The experimental Coulomb displacement energies ΔE_{Coul} with $N > 83$ and $N < 125$, $Z < 81$ are displayed in fig. 4 as differences with respect to calculated spherical contributions, $\Delta E_{\mathrm{Coul}} - \Delta E_{\mathrm{Coul}}^{\mathrm{spherical}}$. The spherical contributions are represented by eq. (4). Various sets of nuclei were considered to calculate the coefficients a and b including (i) all spherical nuclei (near magic numbers) with $Z > 28$ and (ii) the spherical nuclei below and above the region of rare-earth nuclei. The values adopted in fig. 4, $a = 1410$ keV and $b = -603$ keV, were obtained from a least-squares fit to the data displayed in the figure with deformation effects *included* as per eqs. (5) and (6). Data points were used whenever *experimental* values for β_2 were available. Uncertainties of about ± 10 keV near $A = 145$ and ± 25 keV near $A = 200$ in the differences of fig. 4 result from the uncertainty in determining a and b. The increased uncertainty near $A = 200$ is partly the result of an unexplained isotope shift for the Pb isotopes (see below).

Fig. 4 displays the data from this work (filled circles) and from ref.[27]) (open circles). Data with uncertainties ≥ 50 keV were excluded as well as a few data which deviate systematically (^{149}Sm, ^{161}Er, ^{177}Hf; ^{179}Hf also seems to deviate). The earlier and present data including the Gd isotopes display a continuous trend over the entire range. They decrease sharply from $A = 145$ to about 152, followed by a flat region to about $A = 172$ and a gradual increase towards the heaviest nuclei in the region. The energies are indeed decreased strongly by about 130 keV in the region of maximum deformation, $A \approx 166$, which was already noticed earlier[15]).

The curves shown in fig. 4 were calculated for nuclei along the line of stability

defined by eq. (7). The analytical expressions eqs. (5) snd (6) were used to describe the dependence of Coulomb energies on the quadrupole and hexadecapole deformation parameters β_2 and β_4. A simple parameterization [17] mentioned in sect. 5 was used to describe their dependence on proton and neutron numbers Z and N, respectively. The upper curve is calculated assuming $\beta_4 = 0$. The lower curve includes the effect of the hexadecapole deformation β_4. The Coulomb displacement energies are decreased by up to 20 keV in the region $A = 145$ to 160 where β_4 is positive whereas negative values of β_4 in the region $A > 170$ are calculated to have practically no effect on the displacement energies.

The overall agreement between the data and the calculated curves is very good. The low experimental values near $A = 150$ confirm the influence of hexadecapole deformation but the effect seems to be underpredicted by the calculated curves. This behavior is reminiscent of the isotope shift of the nuclear charge radius with its sharp rise beyond $N = 82$ which is also underpredicted [16] by the experimental deformations. Another unexplained feature of the data of fig. 4 is the weak local maximum near $A = 166$. This is the region where the hexadecapole deformation β_4 changes sign, and it was thought [34] that the maximum was related to β_4 on account of the term proportional to β_4^2. However, the term in eq. (5) proportional to β_4^2 is mostly compensated for negative β_4 by the interference term proportional to $\beta_2^2\beta_4$ thus eliminating this explanation.

The basic agreement between the experimental and calculated Coulomb displacement energies suggests that proton core and neutron excess have similar deformations. The reduction if the displacement energies due to deformation would be reduced by a factor of approximately 0.5 if *only* proton core or *only* neutron excess were deformed [30]. The above result seems to contradict the rotationally invariant core model, a special two-fluid model, which successfully describes electric quadrupole moments by assuming that only a fraction of the nucleons participate in the rotational motion [35]. However, recent experiments seem to imply that the neutron deformation of the deformed nuclei ^{152,154}Sm and ^{232}Th are smaller than the proton deformation [36]. The difference appears to be too small, though, to be seen in the present experiment.

Fig. 5 displays the data separately for each sequence of isotopes. The curves are calculated for the respective isotopes using *experimental* quadrupole deformation parameters β_2 and calculated hexadecapole parameters β_4. Again, $\beta_4 = 0$ is assumed for the respective upper curve. The comparison confirms the earlier conclusion that there is global agreement between the data and the calculations provided the same deformation is assumed for proton core and neutron excess. However, local deviations are again apparent. The energies for the Gd isotopes do not decrease as expected from the increase in deformation. The high values for ^{166}Er and ^{168}Er are also not explained. It was hoped that estimates for β_4 could be obtained from such a graph but this is clearly not possible as the influence of individual structures, possibly related to the filling of Nilsson orbits, is superimposed on the general trends.

The uncertainties in establishing the spherical contributions was mentioned earlier. This is particularly apparent for the Pb isotopes where only [205]Pb follows the general behavior displayed in fig. 4 whereas the heavier isotopes are increasingly lower by as much as about 80 keV for [209]Pb. Since this effect cannot be due to deformation, the compatibility of the isotope shift of the Coulomb energies and the charge radii was investigated. Defining the isotope shift coefficient γ_N by [28])

$$\gamma_N = \frac{3A}{R} \frac{\partial R}{\partial N}, \tag{8}$$

where R is the equivalent or rms radius, leads to a simple relationship between the variation with neutron number of the Coulomb energy, the charge radius (proton core) and the neutron excess radius [16,28]:

$$-\gamma_N(\Delta E_{\mathrm{Coul}}) \approx 0.5\gamma_N(\text{p-core}) + 0.5\gamma_N(\text{n-excess}). \tag{9}$$

This equation is strictly valid only for the isotope shift of the *direct* Coulomb displacement energy. The increased sensitivity to the neutron excess is due to the neutron halo. The coefficients are $\gamma_N = \pm 1$ if the quantities vary as $A^{\pm\frac{1}{3}}$. From the experimental Coulomb displacement energies for the Pb isotopes [27] one finds $\gamma_N^{206-208}(\Delta E_{\mathrm{Coul}}) \approx -1.1$ and $\gamma_N^{205-209}(\Delta E_{\mathrm{Coul}}) \approx -1.7$. Thus, ΔE_{Coul} decreases more rapidly than $A^{-\frac{1}{3}}$. Similarly, the isotope shift of the charge radii [4]) is $\gamma_N^{206-208}(\text{p-core}) = 0.73 \pm 0.23$. Thus, $\langle r^2 \rangle^{\frac{1}{2}}$ increases much less rapidly than $A^{\frac{1}{3}}$ (i.e. $A^{0.24}$). Using eq. (9) yields an isotope shift of the neutron excess radii, γ_N(n-excess) = 1.5 to 2.5, which seems too big. The reason for the observed strong decrease of ΔE_{Coul} may instead be a strong dependence on N of one of the many additional contributions to the Coulomb displacement energy [9,13]) (other than the direct energy) which would lower the displacement energy from [205]Pb to [209]Pb by about 100 keV.

6.2. IAS WIDTH AND CROSS SECTIONS AT 0°

The total widths Γ shown in fig. 6 increase strongly with mass number A, particularly for the sequence of Gd and Er isotopes. This behavior is in contrast to that observed for the sequence of Sn and Te isotopes [19]) which display a much weaker increase with A. Also, the widths for the even-A rare-earth nuclei range from 30 to 110 keV whereas those for the even-A Sn and Te are considerably smaller, 10 to 40 keV. The particularly small value for [176]Yb does not follow the general trend and seems to represent an anomaly.

The total width Γ is made up of two components, the escape width $\Gamma^\uparrow$ and the spreading width $\Gamma^\downarrow$. The former leads mostly to T-allowed proton decay; the latter results from mixing with states of isospin $T-1$ and leads mostly to

T-allowed neutron decay. The ratio of escape to total width, $\Gamma^\uparrow/\Gamma$, appears to be small for the even-A Sn and Te isotopes[19]) as well as for the rare-earth nuclei of the present work thus leading to $\Gamma \approx \Gamma^\downarrow$. This conclusion is based on the small escape widths $\Gamma^\uparrow \approx \Gamma_p$ of typically 2–4 keV measured[15]) for nearby odd-A rare-earth nuclei with their increased p-decay energies. It has been argued[11,37,38]) that the spreading widths $\Gamma^\downarrow$ for heavier nuclei is the result of mixing via the charge-dependent Coulomb interaction with the $(T-1)$-component of the isovector giant monopole resonance. A preliminary analysis[39]) of the present data seems to confirm this concept.

The zero-degree charge-exchange cross sections of table 2 and fig. 7 are correlated to some extent with the widths of fig. 6. Again, a strong increase with mass number is indicated for most data, particularly for the sequence of Gd and Er isotopes. However, the cross sections for the Yb isotopes decrease with mass number. A search for systematic effects which might suggest erroneous experimental results including the small width for ^{176}Yb was unsuccessful.

The Lane potential[40]) has been used successfully to reproduce the cross sections of charge-exchange reactions. It follows from this potential that charge-exchange cross sections should approximately be proportional to $(N-Z)/A^2$. Indeed, total cross sections often follow this dependence [e.g. refs. [41,42])], but significant deviations have also been observed [e.g. ref. [19])], particularly if differential cross sections are considered as is the case in the present work. The present data for the rare earth nuclei do not display (not shown) a simple dependence on $(N-Z)$ or $(N-Z)/A^2$, and the neutron-rich Yb isotopes deviate the most. This result may indicate that the filling of Nilsson orbits or the likely contributions from two-step processes are important, and no attempts at extracting a value for the isovector part of the Lane potential have been made.

7. Summary

The $(^3\text{He}, t)$ charge-exchange reaction has been studied on 19 strongly deformed rare-earth targets. Precise Q-values have been determined from the transitions to the isobaric analog states as well as total widths and zero-degree differential cross sections. The Coulomb displacement energies deduced from the data display a very pronounced dependence on nuclear shape. The overall behavior follows closely that expected from the known quadrupole deformation β_2, but the influence of a positive hexadecapole deformation β_4 for the region $A = 145$ to 155 is also apparent. The experimentally observed reduction in this region actually slightly exceeds the expected amount. A small local maximum near $A = 166$ where β_4 changes sign is also not explained. As expected, negative values of β_4 in the heavier deformed nuclei are found to have little effect on the Coulomb displacement energies.

The total isobaric analog state widths Γ are in the range 30 to 110 keV and display a significant increase with neutron excess. The width of the IAS of ^{176}Yb is rather small and seems to present an anomaly. The zero-degree charge-exchange cross sections also display a general increase with neutron excess except for the sequence of Yb isotopes. No simple dependence on neutron excess as would be expected from an approximate application of the well-established Lane potential appears to exist thus suggesting the presence of contributions from other effects including two-step processes.

Excitation energies and cross sections for the reactions ^{12}C(^{3}He, t)^{12}N, ^{16}O(^{3}He, t)^{16}F and ^{28}Si(^{3}He, t)^{28}P have been obtained in the present investigation, and the relative cross sections are discussed.

Appendix

EXPERIMENTAL RESULTS FOR ^{28}P AND ^{16}F

The present experiment provided information about the reactions and the respective final states of ^{28}Si(^{3}He, t)^{28}P, which was used for calibration, and of ^{16}O(^{3}He, t)^{16}F. Oxygen was present in most targets as a contaminant.

The Q-values and excitation energies from the literature are given in table 3. The Q-value for the transition to the ground state of ^{28}P with its uncertainty of ± 3.7 keV was used for calibration. No systematic deviations were observed for any of the excited ^{28}P states thus confirming the excitation energies [24]. Improved uncertainties can be given for two states, 2143 ± 3 keV for the 1^{+} state and 2406 ± 4 keV for the $\leq 2^{+}$ state.

The Q-values for the transitions to all four ^{16}F states were found slightly more positive than expected from the known mass of ^{16}F, ref. [23]. This value was essentially determined from the ^{14}N(^{3}He, n)^{16}F reaction [47]. The strong transitions to the excited 2^{-} and 3^{-} states (see table 3) provided the most reliable values. The result for ^{16}O(^{3}He, t)^{16}F is $Q = -15430 \pm 10$ keV which is 18 ± 10 keV more positive than given earlier (uncertainty ± 14 keV) but only 11 ± 10 keV more positive than a more recent measurement [43] using the (^{3}He, t) reaction (uncertainty ± 6 keV). The uncertainty of ± 10 keV quoted above includes the uncertainties of the respective excitation energies and of the Q-value of the calibration reaction.

TABLE 3

Zero-degree (^{3}He, t) c.m. cross section for targets of ^{28}Si, ^{16}O and ^{12}C

Target nucleus	Final nucleus	$Q^{a, b)}$ (keV)	$E_x{}^{c)}$ (keV)	$J^{\pi c)}$	$\dfrac{d\sigma}{d\Omega}$ (relative)
^{28}Si	^{28}P	-14350.3 ± 3.7	0	3^+	$100^{d)}$
			106 ± 1	2^+	101
			877 ± 2	0^+	18
			1134 ± 0.5	3^+	173
			1313 ± 2	1^+	113
			1516 ± 5	2^+	~ 13
			1567 ± 3	1^+	105
			2104 ± 1	2^+	171
			2143 ± 5	1^+	361
			2216 ± 5	$4^+(3^+)$	~ 10
			2406 ± 5	$\leq 2^+$	62
^{16}O	^{16}F	-15447.6 ± 14.0	0	0^-	2.6
			194 ± 9	1^-	< 0.3
			424 ± 5	2^-	$100^{e)}$
			720 ± 6	3^-	13.8
^{12}C	^{12}N	-17356.6 ± 1.0	0	1^+	$100^{f)}$

$^a)$ Q-values from ref. [23].
$^b)$ Recent redeterminations [43] are $Q = -14358 \pm 6$ keV for ^{28}Si(^{3}He, t)^{28}P and $Q = -15441 \pm 6$ keV for ^{16}O(^{3}He, t)^{16}F.
$^c)$ Excitation energies and spin-parities for ^{28}P from refs. [24,44], for ^{16}F from refs. [45,46].
$^d)$ 18.7 ± 5.6 μb/sr.
$^e)$ 27.0 ± 8.0 μb/sr.
$^f)$ 4.1 ± 1.2 μb/sr.

Table 3 includes the relative and absolute zero-degree cross sections for the three reactions including ^{12}C(^{3}He, t)^{12}N. The ^{28}P spectrum of fig. 1 is dominated by the 1^+ (2143 keV) state which is by far the strongest followed by the 3^+ (1134 keV) and 2^+ (2104 keV) states. Particularly weak are the following states: 0^+ (877 keV), 2^+ (1516 keV), $4^+(3^+)$ (2216 keV) and also $\leq 2^+$ (2406 keV). This behavior is to be contrasted with that displayed in the 18° spectrum obtained by Ramstein *et al.* [24] at 35 MeV. Here, both 3^+ states (0 keV) and (1134 keV), are particularly strong, followed by 2^+ (2104 keV) and $4^+(3^+)$ (2216 keV). Particularly weak are 0^+ (877 keV) and $\leq 2^+$ (2406 keV). The transition to 0^+ (877 keV) is weak in both experiments. The strengths of the $L = 2$ transitions to the 2^+ states scale approximately. However, the relative strengths for the mixed $L = 0$ and $L = 2$ transitions to the 1^+ states suggest strong $L = 0$ contributions for the 1^+ (2143 keV) state. Similarly, the relative strengths for the mixed $L = 2$ and $L = 4$ transitions to the 3^+ states suggests strong $L = 2$ contributions for the 3^+ (1134 keV) state.

The zero-degree cross sections for the transition to the 2^- (424 keV) state in ^{16}F is by far the strongest while the transition to the 1^- (194 keV) state is practically

zero. The transition to the 2^- state is the only one of the four which involves two components, namely $(1p_{\frac{1}{2}}^{-1}, 1d_{\frac{3}{2}})_{J=2}$ coupled to $L = 1$ or $L = 3$. The transition to the 1^- state is not forbidden, but is weakly excited at all angles [46]. It was found in this recent investigation [46] that all experimental distributions are well described by microscopic DWBA calculations.

References

1) H. A. Bethe and R. F. Bacher, Rev. Mod. Phys. **8** (1936) 83;
   H. A. Bethe, Phys. Rev. **54** (1938) 436
2) L. R. Elton, Nuclear radii, Landolt-Börnstein, new series vol. 1/4 (Springer, Berlin, 1967) p. 1
3) R. Hofstadter and H. R. Collard, Nuclear radii, Landolt-Börnstein, new series vol. 1/4 (Springer, Berlin, 1967) p. 21
4) C. W. de Jager, H. de Vries and C. de Vries, Atomic Data and Nucl. Data Tables **14** (1974) 479
5) R. Engfer, H. Schneuwly, J. L. Vuilleumier, H. K. Walter and A. Zehnder, Atomic Data and Nucl. Data Tables **14** (1974) 504
6) R. C. Barrett and D. F. Jackson, Nuclear sizes and structure, (Clarendon, Oxford, 1977)
7) J. D. Anderson and C. Wong, Phys. Rev. Lett. **7** (1961) 250
8) J. Jänecke, in Isospin in nuclear physics, ed. D. H. Wilkinson (North-Holland, Amsterdam, 1969) ch. 8
9) J. A. Nolen and J. P. Schiffer, Ann. Rev. Nucl. Sci. **19** (1969) 471
10) J. W. Negele, Nucl. Phys. **A165** (1971) 305
11) N. Auerbach, J. Hüfner, A. K. Kerman and C. M. Shakin, Rev. Mod. Phys. **44** (1972) 48
12) S. Shlomo, Rep. Prog. Phys. **41** (1978) 957
13) N. Auerbach, V. Bernard and N. Van Giai, Nucl. Phys. **A337** (1980) 143
14) H. Seitz, Nucl. Phys. **A186** (1972) 547
15) N. H. Merril, S. W. Whineray, W. M. Zuk, D. C. Weisser, C. L. Hollas and M. Borsaru, Nucl. Phys. **A216** (1973) 61
16) J. Jänecke, in Atomic masses and fundamental constants 4, ed. J. H. Sanders and A. H. Wapstra (Plenum, New York, 1972) p. 221
17) J. Jänecke, Phys. Lett. **B103** (1981) 1
18) A. G. Drentje, H. A. Enge and S. B. Kowalski, Nucl. Instr. **122** (1974) 485
19) F. D. Becchetti, W. S. Gray, J. Jänecke, E. R. Sugarbaker and R. S. Tickle, Nucl. Phys. **A271** (1976) 77
20) J. C. Vermeulen, J. van der Plicht, A. G. Drentje, L. W. Put and J. van Driel, Nucl. Instr. **180** (1981) 93
21) J. C. Overlay, P. D. Parker and D. A. Bromley, Nucl. Instr. **68** (1969) 61
22) D. R. Goosman, K. W. Jones, E. K. Warburton and D. E. Alburger, Phys. Rev. **C4** (1971) 1800
23) A. H. Wapstra and K. Bos, Atomic Data and Nucl. Data Tables **19** (1977) 215
24) B. Ramstein, L. H. Rosier and C. Jeanperrin, Nucl. Phys. **A317** (1979) 460
25) K. van der Borg, KVI Annual Report (1978) p. 118;
    S. Y. van der Werf, KVI Annual Report (1975) p. 96
26) Program IGPLOT, M. Anderson, University of Michigan, 1978, unpublished
27) W. J. Courtney and J. D. Fox, Atomic Data and Nucl. Data Tables **15** (1975) 141
28) J. Jänecke, Nucl. Phys. **A181** (1972) 49
29) R. P. DeVito, S. M. Austin, W. Sterrenburg and V. E. P. Berg, Phys. Rev. Lett. **47** (1981) 628
30) J. P. Draayer and J. Jänecke, unpublished
31) R. W. Hasse, Ann. of Phys. **68** (1971) 377
32) P. H. Stelson and L. Grodzins, Nucl. Data Tables **A1** (1965) 21;
    S. Raman, W. T. Milner, C. W. Nestor and P. H. Stelson, Proc. Int. Conf. on nuclear structure, Tokyo, (1977) p. 79
33) K. E. G. Löbner, M. Vetter and V. Hönig, Nucl. Data Tables **A7** (1970) 495
34) J. Jänecke, E. H. L. Aarts, A. G. Drentje, C. Gaarde and M. N. Harakeh, Proc. Int. Conf. on nuclear physics, Berkeley (1980)
35) P. C. Zalm and P. J. Brussaard, Z. Phys. **A287** (1978) 265

36) H. Clement, R. Frick, G. Graw, F. Merz, H. J. Scheerer, P. Schiemenz, N. Seichert and Sun Tsu Hsun, Phys. Rev. Lett. **48** (1982) 1082
37) A. Z. Mekjian, Nucl. Phys. **A146** (1970) 288
38) N. Auerbach, Nucl. Phys. **A182** (1972) 247
39) J. Jänecke and M. N. Harakeh, Bull. Am. Phys. Soc. **27** (1982) 704
40) A. M. Lane, Phys. Rev. Lett. **8** (1962) 171; Nucl. Phys. **35** (1962) 676
41) P. S. Miller and G. T. Garvey, Nucl. Phys. **A163** (1971) 65
42) T. Murakami, S. Nashahara, T. Nakagawa, S. Morita, H. Orihara, K. Maeda and K. Miura, Nucl. Phys. **A377** (1982) 163
43) M. N. Harakeh and W. A. Sterrenburg, private communication
44) C. Miehe, Thèse, Strasbourg (1975), unpublished, quoted in ref. [24])
45) F. Ajzenberg-Selove, Nucl. Phys. **A375** (1982) 1
46) W. A. Sterrenburg *et al.*, Phys. Rev. **C**, to be published
47) J. M. Adams, A. Adams and J. M. Calvert, J. Phys. A **1** (1968) 549